Stable and anti-sintering tungsten carbides with controllable active phase for selective cleavage of C–O bonds

Huihuang Fang,[†] Weikun Chen,[†] Lijie Wu,[†] Alberto Roldan,*[‡] Youzhu Yuan*[†]

[†]State Key Laboratory of Physical Chemistry of Solid Surfaces, National Engineering Laboratory for Green Chemical Productions of Alcohols-Ethers-Esters and iChEM, College of Chemistry and Chemical Engineering, Xiamen University, Xiamen, 361005, China

[‡]Cardiff Catalysis Institute, School of Chemistry, Cardiff University, Main Building, Park Place, Cardiff, CF10 3AT, United Kingdom

ABSTRACT: Transition metal carbides (TMCs) are important materials in heterogeneous catalysis. Constructing an active phase by rational carbon insertion to achieve efficient catalytic behavior and prolonging the stability by preventing sintering and structure degradation in redox reactions, especially hydroprocessing, remains challenging yet attracting in nanoscience. This work presents an integrated strategy to synthesize stable tungsten carbide nanoparticles with controllable phase compositions by assembling the metal precursor onto carbon nanotubes (CNTs), wrapping a thin polymeric layer, and following a controlled carburization. The polymer serves as a soft carbon source to modulate the metal/carbon ratio in the carbides and produces amorphous carbon to further stabilize the nanoparticles. The as-built p-W$_x$C/CNT displays more than two- and six-times higher activities for guaiacol hydrogenolysis than those prepared by common temperature-programmed-reduction with gaseous carbon (W$_x$C/CNT-TPR) and carbothermal reduction with intrinsic carbon support (W$_x$C/CNT-CTR) and enhances the stability for more than 150 h. These catalysts also achieve high efficiency on cleavage aryl C–O bonds in lignin-derived aromatic ethers including anisole, dimethylphenol, and diphenyl ether with a robust lifespan.

1. Introduction

Transition metal carbides (TMCs) find important applications in energy storage and transformation such as hydrogen evolution reaction, ammonia synthesis, hydrodeoxygenation (HDO), and isomerization.[1–7] The expansion of the metal lattice by integrating carbon atoms into the interstitial sites of parent metals significantly broadens the metal d-band with a greater density of states (DOS) near the Fermi lever.[1–3] Deviating from the parent metals, the sp hybridized orbitals of metals in carbides move to the surface center to hybridize with the d states from the metal and the s states from the carbon; this implies the redistribution of the DOS giving a noble-metal-like catalytic behaviors with high capacity to donate electrons to adsorbates.[5]

Constructing an active phase by modulating TMC structures is one of the most critical challenges on their design. Researchers have posted the importance of specific phases (e.g. W$_2$C, WC, Mo$_2$C and MoC) towards different catalytic behaviors, preventing the wide application of these cost-efficient materials.[8,9] The most prevailing approach for carbide synthesis is temperature-programmed-reduction (TPR) under gaseous carbon precursors such as CH$_4$, CO and C$_3$H$_8$.[10–12] Unfortunately, the rapid diffusion of carbon through the gas-solid interface is barely suspended, resulting in uncontrollable phases and coke deposition (Scheme 1a).[13,14] These drawbacks risk the serious deterioration in catalytic performance. To this end,

carbothermal reduction (CTR) was proposed to slow down the carbon diffusion in carbide formation by using non-volatile solid carbon source, including carbon supports (e.g. activated carbon, carbon nanotube, carbon nanofiber), polymers and metal-organic Frameworks (MOFs), which aims to improve the quality of as-built TMCs.[7,8,14–19] However, the high carburizing temperature to overcome the thermodynamic and kinetic barriers for carbon insertion always induces unexpecting support degradation and particle sintering (Scheme 1b). The method is also limited to the support choices, uncontrollable phase compositions, small metal-carbon interfaces, and difficulty in controlling particle sizes.[2,9,20] Therefore, the balance between the carbon incorporation and accompanied particle changes is of great importance to be considered.
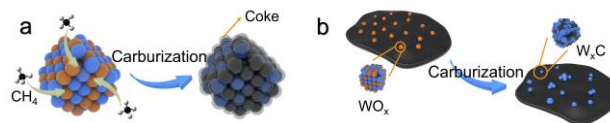
Scheme 1. Illustration of TMCs synthesis via temperature-programmed-reduction (a) and carbothermal reduction (b).

Moreover, the stabilization of TMCs for catalytic applications is another concern. In general, TMCs are exposed to harsh catalytic environment including H$_2$, CO H$_2$O, O$_2$ and oxidants under elevated temperatures and pressures; the redox conditions can easily induce deactivation via surface decon-

struction, phase transition, particle sintering, and coke deposition.[7,16,21–24] Lee found the activity loss in C–O bond scission due to the formation of oxycarbides from Mo$_2$C.[24] Stellwagen identified WO$_2$ in working W$_2$C catalyst during the HDO recycle tests.[16] DFT calculations indicate that raising the C coordination number of metal atoms promotes the stability of TMCs.[25] Li reported the particle agglomeration of metal carbides during the alkylation of methylfuran with mesityl oxide.[26] Jongerius *et al.* also demonstrated the particle sintering as the main reason for catalyst deactivation in guaiacol HDO reaction.[27] The sintering rate is affected by several parameters involving temperature, atmosphere, support, and metal type.[28] Therefore, developing a reliable synthetic strategy for engineering controllable, non-sintered and uniform carbide particles is greatly important and attracting.

Here, we present a simple but powerful strategy to fabricate uniform and stable carbide nanoparticles (NPs) by assembling CNTs and amorphous carbon derived from polymeric layer. Their catalytic performance and stability were tested on the hydrogenolysis of guaiacol and other aromatic ethers, which are typical reactions involving the redox conditions, high temperature and H$_2$ pressure. The as-built p-W$_x$C/CNT via rational carburization and semi-protected by polymer-derived carbon achieved an efficient cleavage of C–O bond with remarkable stability superior to other materials with other synthesis methods. Efforts are devoted to study insight into the role of incorporated polymer precursor as flexible carbon source and the promoting effect of CNTs on stabilizing carbide NPs by characterizing the catalysts through X-ray diffraction (XRD), transmission electron microscopy (TEM), scanning transmission electron microscopy (STEM), X-ray photoelectron spectroscopy (XPS), thermal diffusivity and computational simulations.

2. Experimental section

2.1 Catalyst synthesis

All the chemicals and reagents are of analytical grade and used without any further purification. CNTs were obtained from the Shenzhen Nanotech Port Co., Ltd and pretreated in a 34% HNO$_3$ aqueous solution at 90 °C for 8h to remove residual metallic species. The p-W$_x$C/CNT catalysts were prepared by an integrated method including deposition-precipitation, polymerization, and carburization. In brief, 1 g CNTs and 240 mg anhydrous WCl$_6$ were dissolved in 150 mL ethanol and then dispersed with ultrasonication for 30 min. 5 mL water was added into the solution drop by drop under vigorous stirring and then raise the temperature of the solution to 80 °C and maintained overnight in an oil bath. After cooling down, the obtained solid product, named as WO$_x$/CNT, was collected by centrifuged and washed with ethanol and water before drying at 80 °C for further use. The polymerization procedure was used to wrap the WO$_x$/CNT a polymeric layer (RF layer). Firstly, 100 mg WO$_x$/CNT was dispersed in 100 mL water and then added 250 mg resorcinol and 0.5 mL formaldehyde aqueous solution under stirring and heated to reflux at 85 °C for 24 h to obtain WO$_x$/CNT@RF. The thickness of RF layer is easily controlled by the amount of resorcinol and formaldehyde. To carry out the carburization reaction, the as prepared precursors were pyrolysis and carburized at 850 °C for 0-6 h at an Ar flow rate of 15mL/min to obtained well-controlled phase compositions. For temperature-programmed-reduction, the W$_2$C/CNT-TPR was prepared by carburization of WO$_x$/CNT at 15%CH$_4$-85%H$_2$ flow rate of 15 mL/min at 850 °C for 2 h.

The W$_x$C/CNT-CTR based on the carbothermal reduction was prepared at 900-950 °C for 2-6 h under Ar flow. For comparison, the C-supported tungsten carbide derived from RF polymer was prepared by carburization of organic-inorganic hybrid precursor according our previous reports,[8,29] denoted as W$_x$C@CS(RF). The samples with CNTs incorporation were synthesized by similar methods by adding CNTs and other C materials during the preparation of precursors, denoted as W$_x$C@CS(RF)-CNTs.

2.2 Characterization

The XRD patterns were collected on a Rigaku Ultima IV X-ray diffractometer equipped with Cu–Kα radiation (35 kV and 15 mA) at scanning 2θ from 10° to 90°. The in situ XRD was carried out with a in situ gas flow chamber equipped with thermocouple to monitor the temperature. The obtained data were analyzed by JCPDS database and the XRD Rietveld refinement was carried out by Topas software to analyze the phase compositions.

TEM and HAADF-STEM images were acquired from a Philips Analytical FEI Tecnai 20 electron microscope operated at an acceleration voltage of 200 kV. Fresh samples were ultrasonically dispersed, dropped and dried on copper grids.

XPS profiles were obtained on an Omicron Sphera II photoelectron spectrometer equipped with an Al–Kα X-ray radiation source (hν = 1486.6 eV). Prior to the test, the samples were freshly pretreated in a in situ chamber to ensure theses samples are in similar chemical state with fresh ones before activity testing. Then the samples were transferred to the XPS analysis chamber after cooling down under vacuum. The binding energy was calibrated using the C 1s peak at 284.5 eV.

Thermal diffusivity was tested on an NETZSCH LFA457/2/G by a laser flash method under a nitrogen atmosphere in the temperature range of 312–352 K.

Argon sorption was carried out to measure the specific surface area, pore volume and average pore diameter on a Micromeritics 2020.

2.3 Catalytic test

The hydrogenolysis of guaiacol and other aromatic ethers were evaluated on a continuous flow fixed bed reaction with a computer-controlled autosampling system. Briefly, 200 mg of fresh catalyst was sandwiched into the center of the quartz tubular reactor with quartz wool. Prior to the test, the catalysts were pretreated at 450 °C for 4 h under 5% H$_2$/N$_2$. The catalyst bed was cooled down to the target reaction temperature, and pure H$_2$ was fed into the reactor at 3.0 MPa. Liquid guaiacol and other aromatic ethers were pumped into the reactor through a Series III digital HPLC pump (Scientific Systems, Inc.) with required weight liquid hourly space velocity (WLHSV). The products were analyzed online using an Agilent 7890A gas chromatograph (GC) equipped with an autosampling value, flame ionization detector, and a DB-Wax capillary column. A GC 2060 with thermal conductivity detector and a TDX column were used to analyze gas products (CH$_4$, CO, CO$_2$, and H$_2$O). Detailed guaiacol conversion and product selectivity were calculated by equations as follows: (1) Conversion = {(moles of guaiacol)$_{in}$ – (moles of guaiacol)$_{out}$}/ (moles of guaiacol)$_{in}$ × 100%; (2) Selectivity = moles of ring product i / the sum moles of guaiacol consumed × 100%. Unless otherwise noted, the carbon balance was about 95% ± 2%.

2.4. Computational Details

We performed systematic density functional theory simulations of W_XC on pristine and defective graphite as support. These models represent the different catalysts in terms of source of C, thus the WC_x/CNT@RF is modelled using a pristine graphene support while CNT-TPR and CNT-CTR are represented by a single and double carbon vacancy support (see **Figure 1**). The reaction energy for decarbonization under a reductive environment (e.g. in presence of H_2) was calculated using following the reaction in **Eq X**.

$$WC_X + 2.H_2 \rightarrow WC_{X-1} + CH_4 \qquad \textbf{Eq X}$$
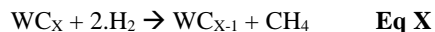
Spin-polarized, periodic plane-wave density functional theory calculations were performed with the Vienna Ab Initio Simulation Package (VASP 5). The density functional of revised Perdew, Burke, and Ernzerhoff (RPBE) was used to calculate exchange and correlation contributions including long-range interactions with Grimme's empirical dispersion correction DFT-D3. Projector-augmented wave (PAW) pseudopotentials as implemented in VASP were used to describe the core electrons. A kinetic cut-off was set at 550 eV was employ ensuring no Pulay-stress. Dipole corrections as implemented in the VASP code were applied perpendicular to the surfaces upon adsorption WC dimer adsorption. The number of k-points was benchmarked and adjusted to density of 0.3 Å^{-1}.

For modelling the pristine graphite support, a one C-layer exposing the (0001) surface with 72 carbon atoms was created. The single and double vacancies were derived from the pristine one by removing one and two contiguous carbon atoms respectively following by atomic relaxation. These support models expose a surface area of 189.6 Å^2 with a perpendicular vacuum gap of 30 Å ensuring no spurious interaction with periodic images.
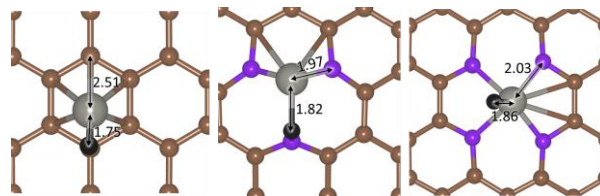

Figure 1. Schematic representation of WC supported on (left) pristine, (center) single vacancy and (right) double vacancy graphite. Color scheme: brown is C-graphite, blue is uncoordinated C-graphite, grey is W and black is C from WC. Average distances are displayed in Å.
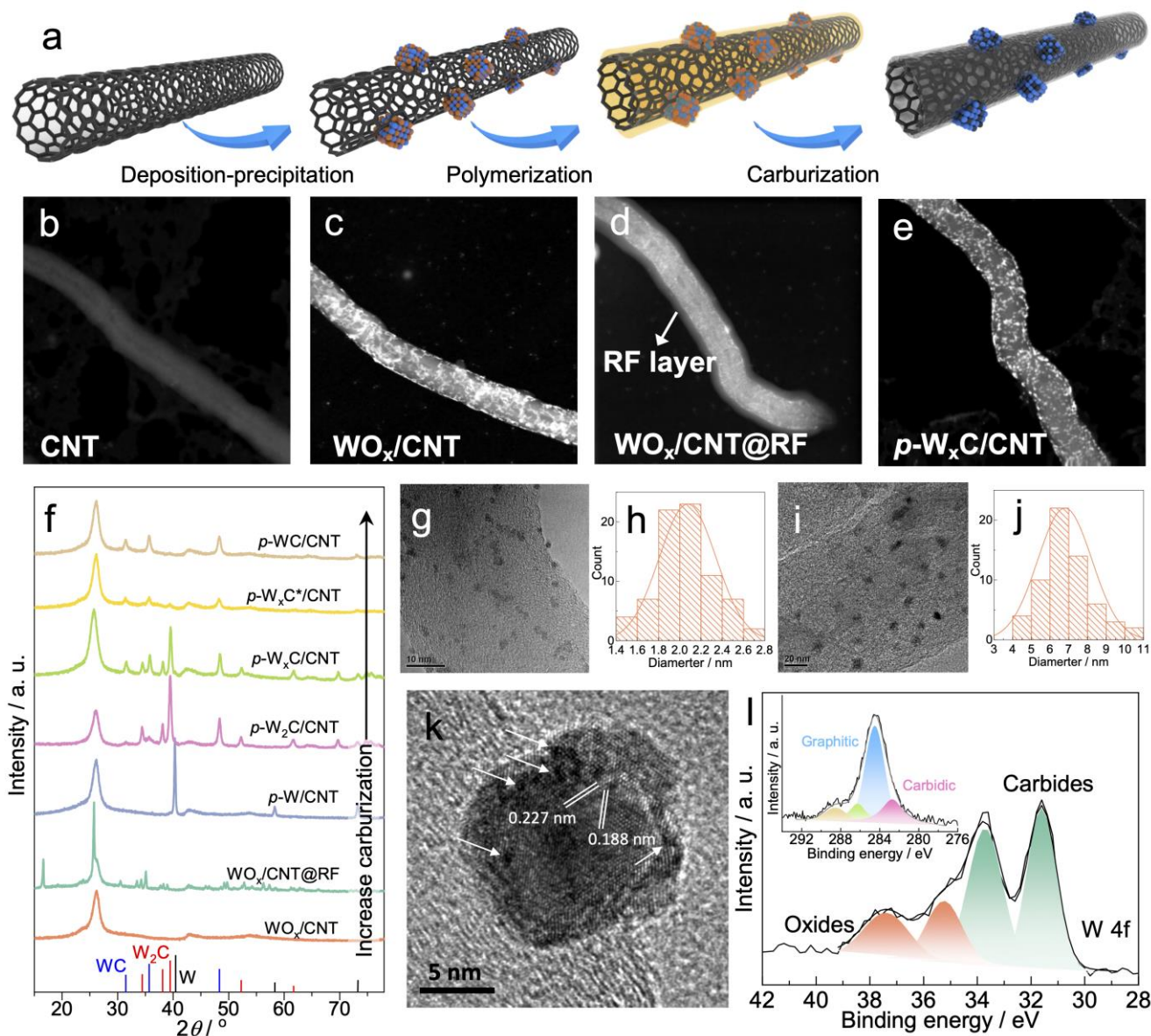
Figure 1. (a) Schematic illustration for preparation of p-W$_x$C/CNT involving deposition-precipitation, polymerization by Stöber method, and rational pyrolysis and carburization; (b-e) STEM images of CNTs, WO$_x$/CNT, WO$_x$/CNT@RF and p-W$_x$C/CNT; (f) XRD patterns of the as-prepared precursors and samples with different carburizing degrees; (g-j) TEM images and particle size distributions of WO$_x$/CNT and p-W$_x$C/CNT, respectively; (k) HR-TEM images of p-W$_x$C/CNT; (l) W 4f and C 1s (insert) XPS profiles of p-W$_x$C/CNT.

3. Results and discussions

3.1 Construction of uniform tungsten carbide particles with well-controlled phases

Fig. 1a shows the integrated strategy to fabricate uniform and stable tungsten carbide NPs onto the CNTs, involving the deposition of metal precursors on CNTs, polymerization by Stöber method, and rational carburization. The CNTs were pretreated in concentrated HNO$_3$ solution to provide surface function groups, confirmed by C 1s XPS in Fig. S1, for anchoring of metal precursor and organic species during the Stöber procedure. WCl$_6$ was used as active tungsten precursor to react with ethanol first, forming a stable intermediate of WCl$_3$(OC$_2$H$_5$)$_2$. This was followed by deposition of tungsten oxides onto the CNTs through hydrolysis of the intermediate. The obtained WO$_x$/CNT was further coated with a polymeric layer of resorcinol/formaldehyde (RF) by Stöber method,

hereafter denoted as WO$_x$/CNT@RF. The formaldehyde reacts with resorcinol to produce hydroxymethyl substituted species and then form RF layer after ageing. See more details in the experimental section. Subsequently, the WO$_x$ particles were transformed into carbide NPs with controlled carburization over specific heating rate and carburizing time. It is expected that carbon atoms originated from RF diffuse into the interstitial sites of tungsten matrix easily during the pyrolysis and carburization. This is due to the flexible carbon framework in RF and the closed interaction between the tungsten species and carbon source. As a result, well-controlled tungsten carbides were synthesized with uniform dispersion.

The STEM image in Fig. 1b shows pristine CNTs with an outer diameter of approximate 50 nm. The WO$_x$ species are clearly visible after deposition-precipitation (Fig. 1c). The magnified image from TEM image demonstrates ultra-small particles embedded on the CNTs with a diameter of average 2

nm (Fig. 1g and h). Fig. 1d reveals the formation of a thin RF layer as 1D shell wrapping the CNTs, indicating the successful polymerization. Interestingly, the pyrolysis and carburizing process allow the exposure of the uniform particles with the disappearance of the RF layer (Fig. 1e). Slight increase in the particle size in the range of 4-9 nm by analysis of the size distribution (Fig. 1i and j). This is due to the lattice expansion by carbon insertion to the tungsten matrix and coalescence of small particles.

Combining the flexible RF layer as the carbon source allows the synthesis of carbide NPs with high degree of compositional control, as shown in XRD patterns (Fig. 1f). No obvious diffractions could be found from initial WO_x/CNT except the typical peaks ascribed to CNTs. A set of new diffraction peaks was newly visible from $WO_x/CNT@RF$ due to the formation of RF layer by polymerization. At the initial stage of pyrolysis, the WO_x NPs were reduced into metallic W NPs as shown by the typical diffraction peaks located at 40.42°, 58.36°, and 73.33°, hereafter denoted as p-W/CNT. Further carburization allows the carbon to diffuse into the interstitial sites of tungsten matrix, forming W_2C, semi-carburized W_xC and pure WC. It is worth noting that, the flexible carbide compositions were easy to achieve by controlling the carburization conditions. Fig. 1k shows the HR-TEM images of typical W_xC NPs in p-W_xC/CNT and it exhibits clear lattice fringes with interplanar distances of 0.188 and 0.227 nm, corresponding the (101) and (100) facets of W_2C and WC, respectively. More interestingly, dark spots were observed (marked by white arrows), ascribed to the C vacancies on the surface of NPs, which are capable of trapping and activating reactants. The represented XPS profile of W 4f (Fig. 1l) is featured with two pronounced peaks centered at 31.7 eV and 33.8 eV, typical of tungsten carbides. The C 1s (Fig. 1l-insert) displays a broad peak compared with that of initial CNTs (Fig. S1) which deconvoluted peak at 282.2 eV confirms the formation of carbide species. These results coincide with the XRD patterns and TEM analysis.
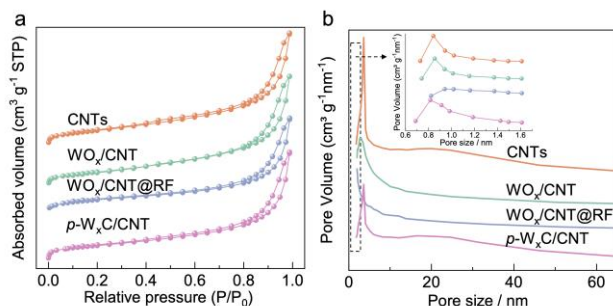

Figure 2. (a) Argon adsorption-desorption isotherms; (b) pore size distributions.

The specific surface area and pore structure through Ar sorption (Fig. 2 and Table S1) were further investigated to understand the evolution of the catalyst along its synthesis. The argon adsorption-desorption isotherms are identified as a type II isotherm that display H3-hysteresis loop at a P/P_0 range of 0.30–0.99, suggesting the presence of mesoporous structure and large BET surface area on these CNTs-based materials (Fig. 2a). CNTs exhibit a large surface area of 100.6 m^2 g^{-1} while WO_x/CNT show slight decrease of surface area with 91.6 m^2 g^{-1} after loading W precursors. A significant decline on the surface area was found upon formation of the polymeric

layer in $WO_x/CNT@RF$ (69.7 m^2 g^{-1}). The final pyrolysis and carburization stage drove the destruction of the RF layer and the return to a high surface of 100.4 m^2 g^{-1}, allowing the exposure of carbide NPs. The pore distribution was further analyzed in Fig. 2b. CNTs display abundant pores of 2–4 nm and 15–40 nm, belonging to the external interstitial pores and the internal pores of CNTs, respectively, facilitating the trap of metal species. It can be seen that the mesopores disappeared after wrapping of RF layer and reappear after pyrolysis and carburization, coinciding with results of surface area and TEM.

3.2 Importance of RF layer for controlling the phase compositions of and stabilizing the particle size of tungsten carbides

To prepare well-defined metal carbides, the choice of carbon source is important as it extensively influences the structures, the surface properties, and the particle sizes. Although the gaseous carbon source like CH_4 allows the formation of carbides simply, the coke deposition and massive C-terminations are also produced, greatly deterring the catalytic performance. Suitable solid carbons including carbon supports,[2,7,14] polymers,[8,29] carbon containing chemicals[1,18] and MOFs[17] were applied in carbide synthesis.[2] Solid carbon supports such as activated carbon, CNTs and CNF slow down the carbon diffusion into metal species because of the need to break the C–C bonds from graphitic carbon fragments. The strong C–C bonding and the small metal-carbon interface drive great difficulty in surface and structural engineering even at elevated temperatures. On the other hand, polymers and metal-organic precursors like RF and MOFs stand out their advantages in controllable carburization due to the closed contact between the metal and carbon containing chemicals as well as the flexible carbon originating from organic molecules, which is easier to produce carbon atoms for carburization. However, the loose structure of carbons from these precursors lead to support degradation under carburization conditions facilitating the particle agglomeration and sintering. Therefore, it is important to balance the carburization engineering and stabilization of particles.
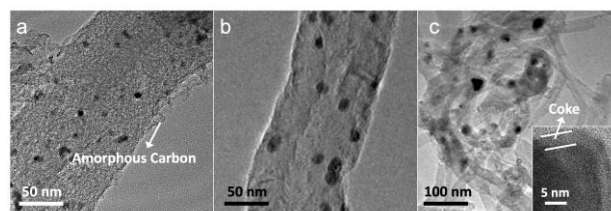

Figure 3. TEM images of (a) p-W_xC/CNT; (b) W_xC/CNT-CTR; (c) W_xC/CNT-TPR.

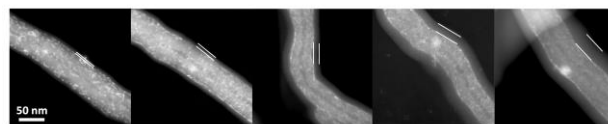**Figure 4.** STEM images of $WO_x/CNT@RF$ with increasing thickness of RF layers.

Fig. 3 shows the TEM images of CNT supported tungsten carbide NPs with different synthesis methods. Fig. 3a exposes the typical TEM image of p-W_xC/CNT by our proposed strategy and it shows that the wrapping RF layer serves as the flexible carbon source for carburization and transforms into amor-

phous carbon; the fragments were attached on the surface of CNTs and the tungsten carbide NPs were semi-protected. The obtained particles maintain an ultra-small scale even after high-temperature pyrolysis and carburization. For comparison, the sample prepared by common carbothermal reduction using CNT support as the only carbon precursor, denoted as W_xC/CNT-CTR, displays much larger particles, which is ascribed to the particle agglomeration during the carburization process (Fig. 3b). As evidenced in Fig. S2, the XRD patterns remains similar with different carburizing conditions and the carbide compositions are out of control with mixed metal and carbide phases even under 950 °C for 6h. This is due to the difficulty of C diffusion from CNT matrix and the small metal-carbon interface. On the other hand, W_xC/CNT-TPR prepared by the temperature-programmed-reduction under 15%CH_4-85%H_2 in Fig. 3c shows quite large particle size (20–40 nm), which are identified as W_2C phase from the XRD pattern (Fig. S3). Although the W_2C is still not further transformed into W_xC and WC, the disassociation of CH_4 on gas-solid interaction allows the deposition of coke on carbides leading to a thick carbon layer (approximately 3–5 nm) coating on the outer surface of carbide NPs. The carbon deposition blocks and prevents the exposure of active sites, negatively influencing the catalytic performance. Previous studies show that the carburization conditions have a large influence on the phase and the particle size when using TPR and CTR methods.[2,9] Therefore, it is challenging to consider the effect of metal loading, temperatures, heating rate, carburization time and gas atmosphere. It is worth highlighting that our established strategy combines the CNTs as the support and the RF layer as the flexible carbon precursor allowing a selective carburization to form ultra-small particles with controllable carbide compositions.

The results from the computational analysis clearly align with the above experimental observations. The reaction energy for hydrogen-decarburization increases (in absolute value) with the number of support defects, i.e. double vacancy (E_R= -4.2 eV) > single vacancy (E_R= -3.5 eV) > pristine (E_R= -2.6 eV). The thermodynamically favorable decarburization of W_xC leads to a competition with the guaiacol hydrogenation. Hence, the very exothermic decarburization of W_xC supported on C-defective CNT-TPR and CNT-CTR promotes the deactivation of the catalysts while using the RF as carbon source nurture the support stabilizing the catalysts.

Moreover, the wrapping of the RF layer is a well-controlled manner, and the thickness of the RF layer can be simply modulated by adding the amount of resorcinol and formaldehyde, as shown in Fig. 5. This RF layer depends on the demand of metal loading and carburizing degree, aiming to synthesize rational carbides for specific reactions. As demonstrated in Fig. S4, ultra-small and semi-protected tungsten carbide NPs can be fabricated with thin RF layer with massive particle concentration (Fig. S4a); too thick RF layer results in coating of these as-prepared particle which might suppress their catalytic performance (Fig. S4b). The RF layer not only provides flexible carbon insertion into tungsten matrix during the pyrolysis and carburization, but also forms amorphous carbons to further anchor carbide particles in the surrounding. Here we believe that similar physical confinement can also be in effect via strong interaction between tungsten precursors and CNT supports.

To obtain further insights into the role of the RF layer on the phase compositions under a catalytic reducing atmosphere, in situ XRD measurements were conducted under H_2 at different temperatures. Fig. 5a demonstrates the XRD patterns of p-W_xC/CNT in the range of 600–850 °C under H_2. It can be seen that the formation of W diffraction started from 700 °C and became the sharpest at 750 °C with the decrease of W_2C peaks, which is due to the decarburization via the reaction of H_2 with interstitial carbons. However, the W peaks decreased again with further increase of temperatures. For analysis of the phase compositions, XRD Rietveld refinement was carried out in Fig. 5a-right. Only 2 wt.% W was found with 56 wt.% W_2C and 42 wt.% WC in the sample at 600 °C under H_2 treatment. The W content displayed a volcano curve and reached the maximum at 750 °C. W_2C and WC contents show reverse trends. These results indicated that a reversible decarburization and recarburization occurred in p-W_xC/CNT during the high-temperature treatment under H_2, which is beneficial for maintaining carbide phases. In contrary, the W_xC/CNT-CTR without RF wrapping showed easier decarburization at the same temperature (Fig. 5b), i.e. the intensity of W diffraction increased greatly with the decrease of W_2C and WC. The refinement results showed that the W content increased from 12 to 50 wt.% in the range of 600–850 °C while the W_2C and WC content decreased from 47 to 21 wt.% and from 41 to 29 wt.%, respectively. That is to say, the gasification of carbons from carbide is much easier than that carbon insertion from CNTs under H_2, which is quite different with p-W_xC/CNT. Therefore, the RF-derived carbon serves as a more flexible carbon source for reversible carburization under reducing atmosphere, which is important to keep active catalytic phases in specific reactions.
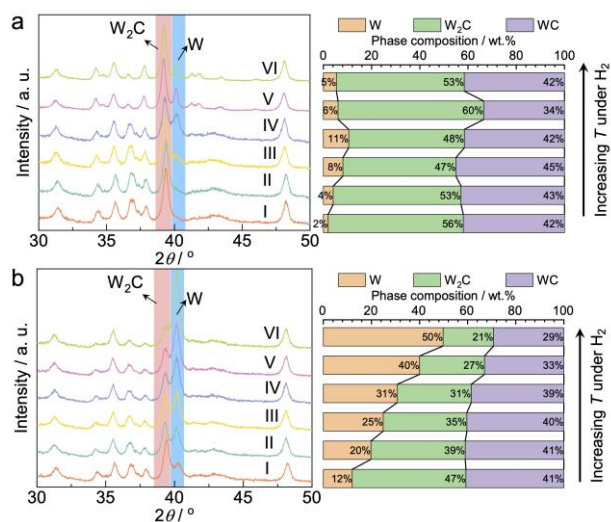

Figure 5. In situ XRD patterns (left) and XRD Rietveld refinement analysis (right) of (a) p-W_xC/CNT and (b) W_xC/CNT-CTR with the increase of temperature under H_2; (I) 600 °C, (II) 650 °C, (III) 700 °C, (IV) 750 °C, (V) 800 °C, (VI) 850 °C.

3.3 Catalytic performance and stability

We further investigated the catalytic performance and stability of aryl C–O bond cleavage in guaiacol hydrogenolysis because it is a selectivity-sensitive reaction on active carbide phases (Scheme S1).[29] As shown in Fig. 6a, the phenol selec-

6

tivity via direct hydrogenolysis of aryl C–O bond depends on the phase control of tungsten carbides. The p-W/CNT facilies the formation of catechol through breaking the aliphatic C–O bond with only 10.2% guaiacol conversion. Small amount of produced phenol is presumably due to the carbon modification on metal tungsten during pyrolysis of p-W/CNT. p-W$_2$C/CNT, containing mostly W$_2$C phase, is capable for cleavage of aryl C–O bonds including Ar–OCH$_3$ and Ar–OH to obtain phenol, anisole and benzene without control. Rational carburization on specific compositions on p-W$_x$C/CNT achieve the high phenol selectivity with best guaiacol conversion. Further complete carburization in p-WC/CNT suppresses the catalytic performance. These catalytic results enhance the importance of a controlled phase compositions on metal carbides towards specific reactions.
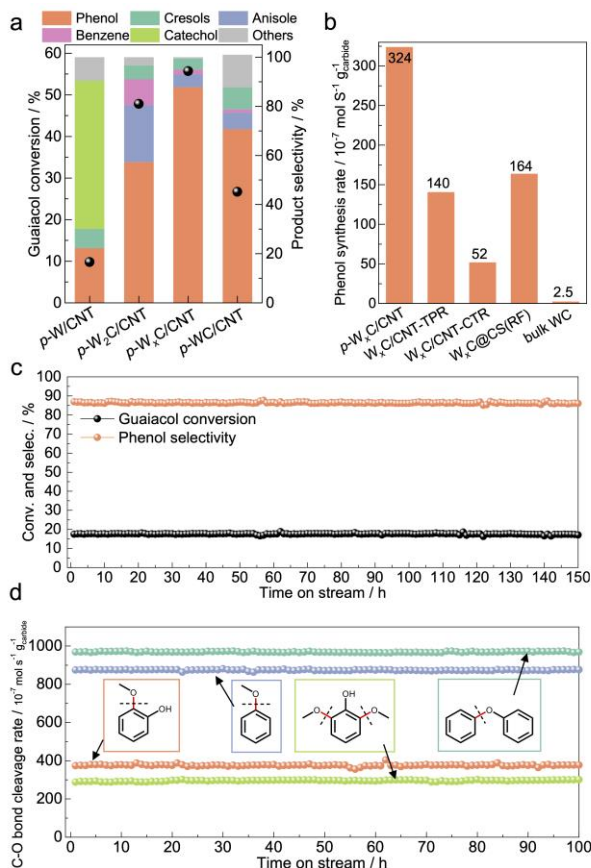

Figure 6. (a) Catalytic performance of guaiacol hydrogenolysis over W-based catalysts with different carburizing degrees; (b) comparison of phenol synthesis rates over the tungsten carbide catalysts with different preparation methods; (c) the catalytic stability of p-W$_x$C/CNT in the hydrogenolysis of guaiacol up to 150 h; (d) rate of C–O bond cleavage on lignin-derived aromatic ethers. Reaction conditions: P(H$_2$) = 3.0 MPa, H$_2$/guaiacol molar ratio = 50; T = 300 °C for guaiacol, 250 °C for anisole and diphenyl ether, and 350 °C for dimethoxyphenol; weight liquid hourly space velocity (WLHSV) = 3.0 h^{-1} for (a), (b) and 9 h^{-1} for (c), (d).

Fig. 6b and Table S2 illustrates the comparison of catalytic performance from samples prepared with different methods. The p-W$_x$C/CNT displays undoubtedly the highest rate with 324 × 10^{-7} mol s^{-1} g$_{carbide}$$^{-1}$, while, in contrast, W$_x$C/CNT-TPR

displays less than half rate (140 × 10^{-7} mol s^{-1} g$_{carbide}$$^{-1}$). This is due to larger carbide particle size and massive coke deposition when CH$_4$ is used as carbon source. W$_x$C/CNT-CTR via direct insertion of carbons from CNTs shows much lower phenol synthesis rate and the formation of catechol (Table S1), which always occurs in the presence of metal tungsten. Although no tungsten diffraction was found and mixed carbides phases, the XPS analysis further confirmed that there is high metal content on the outer surface of particles (Fig. S5). This is ascribed to the small carbon-metal interface during the carburization. It is worth noting that the W$_x$C@CS(RF) demonstrates a satisfying phenol synthesis rate of 164 × 10^{-7} mol s^{-1} g$_{carbide}$$^{-1}$. W$_x$C@CS(RF) is the carbon sphere supported tungsten carbide derived from carburization of the hybrid of RF polymer and tungsten precursor, according our previous reports.[8,29] These results highlight the advantages of RF polymer as a carbon source for carburizing control.

The results of stability tests are shown in Fig. 6c and Fig. S6-8. The p-W$_x$C/CNT exhibits the highest stability under both WLHSV of 3 and 9 h^{-1}. No changes in the activity for more than 150 h time on stream were found (Fig. 6c), while W$_x$C/CNT-TPR shows obvious decrease on the guaiacol conversion with slight suppress of phenol selectivity (Fig. S7). On the other hand, W$_x$C/CNT-CTR is unstable and deactivates soon with the increase of catechol selectivity (Fig. S8), which correlates to the in-situ XRD analysis. Therefore, the introduction of RF layer as the carbon source is beneficial for controlling and stabilizing the active phases of tungsten carbides. To identify the application of p-W$_x$C/CNT, Fig. 6d shows the catalytic performance and the stability on the aryl C–O bonds cleavage in lignin-derived aromatic ethers. The p-W$_x$C/CNT shows high activity on the hydrogenolysis of anisole and diphenyl ether, obtaining approximate 860 and 970 ×10^{-7} mol s^{-1} g$_{carbide}$$^{-1}$. Guaiacol and dimethylphenol display, respectively, an approximate 380 and 290 ×10^{-7} mol s^{-1} g$_{carbide}$$^{-1}$ under optimal reaction temperatures with a WLHSV of 9 h^{-1}. In all cases, no obvious changes in the aryl C–O cleavage rates were found and the p-W$_x$C/CNT maintains at a stable performance throughout the entire 100 h reaction on stream. These results indicate the advantages of our strategy to prepare robust and efficient catalyst towards hydrogenolysis of aryl C–O bonds.

Further analysis of the catalysts from our computational models shows a huge effect of the support carbon vacancies on the electronic structure and electrostatic local potentials. The left column in Figure X represents the electron charge density difference of WC upon deposition on the graphite models and indicates that the carbon defect relocates the W electron density towards the surface – as more C-defects more density displacement away from the catalytic surface. The effect is clearer once the local potential is projected on the electron density. This electrostatic potential allows to graphically identify sites with high (and low) electron density, which can indicate potential (electrostatic) interaction sites of the W$_x$C clusters with molecules. For instance, the oxo groups resulting from the C–O cleavage would favorably adsorb on electron rich sites such the W supported on pristine graphite (Fig Xa) while the same oxo group would avoid electron depleted sites (e.g. Fig Xc). This information added to the competitive hydrogenation reactions described above enhance the importance of the graphitic support integrity for an active and durable catalysts.
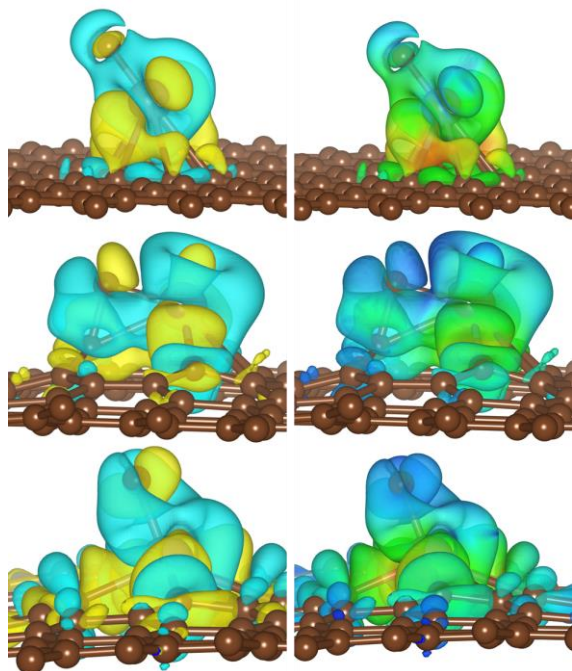
Figure X. (left) electron charge difference (iso-value at 0.003 eV·Å^{-3}) and (right) projection of the electrostatic local potential on the electron charge difference of WC supported on (a) pristine, (b) single vacancy and (c) double vacancy graphite model. Yellow iso-surface indicates electron charge accumulation, and the local potential has a color scale between blue (negative) and red (positive).

3.4 Promoting effect of CNTs incorporation

CNTs are attractive materials because of their unique thermal, mechanical and electronic properties. To identify the effect of CNTs on the high activity and robust stability of p-W_xC/CNT, we prepared the $W_xC@CS(RF)$ using the pyrolysis and carburization of organic-inorganic hybrid precursors as previously reported.[8,29] The polymer derived from the polymerization of resorcinol with formaldehyde in the presence of tungsten precursor. $W_xC@CS(RF)$ displays expectational catalytic activity at the initial stage (Fig. S9). However, the catalyst rapidly deactivates after 5 h on stream. $W_xC@CS(RF)$-CNTs was prepared by CNTs incorporation during the synthesis of hybrid precursors. Interestingly, the catalyst displays a similar performance but prolongs the lifespan under the same reaction conditions (Fig. S10). No obvious changes in guaiacol conversion and phenol selectivity were found after 100 h reaction. Upon increasing the WLHSV from 3 to 9 h^{-1}, the catalyst gradually deactivates at one third of the initial conversion with slight decrease of phenol selectivity (Fig. S11). These results prove the CNTs ability to promote the stabilization of catalyst's performance.

To further investigate the changes of catalyst structures during the HDO reaction, TEM images at different stages were conducted (Fig. 7). The TEM image of $W_xC@CS(RF)$ in Fig. 7a shows a degradation of the carbon support with obvious particle sintering after 8 h reaction. The sintering situation is more serious after 16 and 24h of reaction. This is also confirmed by the XRD analysis where the used catalyst displays similar but sharper diffractions peaks (Fig. S12). Importantly, Fig. 7b well-dispersed NPs in $W_xC@CS(RF)$-CNTs with slight agglomeration during the reaction process. The particles remained practically with the same size after the 96 h of reaction. Further XRD analysis demonstrates no significant changes in both diffractions' peaks and their sharpness (Fig. S13). As depicted in Fig. 8, thermal diffusivity was carried out indicating that the CNTs-incorporated samples demonstrated higher thermal diffusivity with the trend: p-W_xC/CNT > $W_xC@CS(RF)$-CNTs > CNTs > $W_xC@CS(RF)$. Thus, the high thermal diffusivity facilitates the dissipation of heat from the exothermic reaction and retards the particle sintering. Thus, the CNTs serve as excellent candidates for anchoring and stabilizing the carbide NPs.
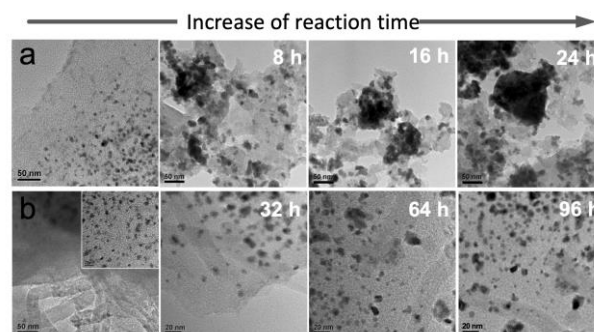

Figure 7. TEM images of (a) $W_xC@CS(RF)$ and (b) $W_xC@CS(RF)$-CNTs with an increase of reaction time on stream.
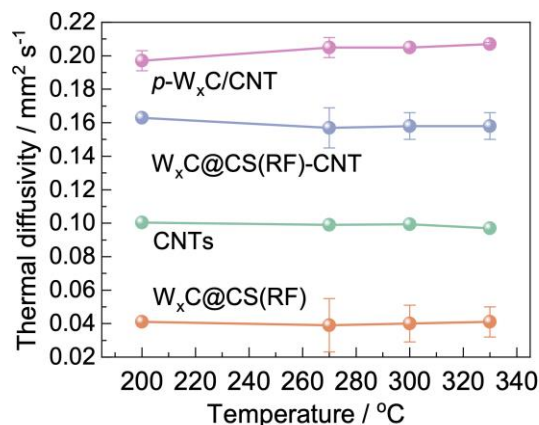
Figure 8. Thermal diffusivity of CNTs, $W_xC@CS(RF)$, $W_xC@CS(RF)$-CNTs and p-W_xC/CNT under different temperatures.

4. Conclusions

Stable and well-controlled tungsten carbide catalysts have been successfully synthesized by assembling the CNTs, RF layer and tungsten precursors. Wrapping a RF layer with closed contact with tungsten species allows control over the carbide phase compositions of robust and small carbide NPs, which, anchored on CNTs, minimize the particle sintering during synthesis and reaction process. The well-controlled p-W_xC/CNT displays a significant activity on guaiacol hydrogenolysis with 324×10^{-7} mol s^{-1} g$_{carbide}^{-1}$ at 300 °C, which is two- and six-times higher than those catalysts prepared by common TPR and CTR methods, and maintain their perfor-

mance for more than 150 h of stream reaction. This catalyst also provided satisfying efficiency on the aryl C–O bonds cleavage in anisole, dimethylphenol, and diphenyl ether with a stable reaction lifespan. The tolerance of H_2 atmosphere and particle sintering were proved to achieve the p-W_xC/CNT with ultra-stability. This work presents a viable way to construct a stable carbide catalyst with well-controlled phase compositions for heterogeneous catalysis involving thermo-, electro-, and photo-chemical reactions.

ASSOCIATED CONTENT

Supporting Information

The Supporting Information is available free of charge on the ACS Publications website.

AUTHOR INFORMATION

Corresponding Author

* Alberto Roldan, RoldanMartinezA@cardiff.ac.uk;
* Youzhu Yuan, yzyuan@xmu.edu.cn.

Present Addresses

†State Key Laboratory of Physical Chemistry of Solid Surfaces, National Engineering Laboratory for Green Chemical Productions of Alcohols-Ethers-Esters and iChEM, College of Chemistry and Chemical Engineering, Xiamen University, Xiamen, 361005, China

‡School of Chemistry, Cardiff University, Main Building, Park Place, Cardiff, CF10 3AT, United Kingdom

ACKNOWLEDGMENTS

REFERENCES

(1) Zhong, Y.; Xia, X. H.; Shi, F.; Zhan, J. Y.; Tu, J. P.; Fan, H. J. Transition Metal Carbides and Nitrides in Energy Storage and Conversion. *Adv. Sci.* **2015**, *3*.

(2) Pang, J.; Sun, J.; Zheng, M.; Li, H.; Wang, Y.; Zhang, T. Transition Metal Carbide Catalysts for Biomass Conversion: A Review. *Appl. Catal. B Environ.* **2019**, *254*, 510–522.

(3) Cheng, H.; Ding, L. X.; Chen, G. F.; Zhang, L.; Xue, J.; Wang, H. Molybdenum Carbide Nanodots Enable Efficient Electrocatalytic Nitrogen Fixation under Ambient Conditions. *Adv. Mater.* **2018**, *30*, 1–7.

(4) Xu, Y.T.; Xiao, X.; Ye, Z.-M.; Zhao, S.; Shen, R.; He, C.T.; Zhang, J.P.; Li, Y.; Chen, X.M. Cage-Confinement Pyrolysis Route to Ultrasmall Tungsten Carbide Nanoparticles for Efficient Electrocatalytic Hydrogen Evolution. *J. Am. Chem. Soc.* **2017**, *139*, 5285–5288.

(5) Lin, Z.; Chen, R.; Qu, Z.; Chen, J. G. Hydrodeoxygenation of Biomass-Derived Oxygenates over Metal Carbides: From Model Surfaces to Powder Catalysts. *Green Chem.* **2018**, *20*, 2679–2696.

(6) Lu, Q.; Chen, C. J.; Luc, W.; Chen, J. G.; Bhan, A.; Jiao, F. Ordered Mesoporous Metal Carbides with Enhanced Anisole Hydrodeoxygenation Selectivity. *ACS Catal.* **2016**, *6*, 3506–3514.

(7) A. W. Hollak, S.; W. Gosselink, R.; S. van Es, D.; H. Bitter, J. Comparison of Tungsten and Molybdenum Carbide Catalysts for the Hydrodeoxygenation of Oleic Acid. *ACS Catal.* **2013**, *3*, 2837–2844.

(8) Fang, H.; Roldan, A.; Tian, C.; Zheng, Y.; Duan, X.; Chen, K.; Ye, L.; Leoni, S.; Yuan, Y. Structural Tuning and Catalysis of Tungsten Carbides for the Regioselective Cleavage of C–O Bonds. *J. Catal.* **2019**, *369*, 283–295.

(9) Hunt, S. T.; Nimmanwudipong, T.; Román-Leshkov, Y. Engineering Non-Sintered, Metal-Terminated Tungsten Carbide Nanoparticles for Catalysis. *Angew. Chemie* **2014**, *126*, 5231–5236.

(10) Lemaître, J.; Vidick, B.; Delmon, B. Control of the Catalytic Activity of Tungsten Carbides: I. Preparation of Highly Dispersed Tungsten Carbides. *J. Catal.* **1986**, *99*, 415–427.

(11) Miller, R. L.; Wolczanski, P. T.; Rheingold, A. L. Carbide Formation via Carbon Monoxide Dissociation Across a W≡W Bond. *J. Am. Chem. Soc.* **1993**, *115*, 10422–10423.

(12) Hunt, S. T.; Milina, M.; Alba-Rubio, A. C.; Hendon, C. H.; Dumesic, J. A.; Román-Leshkov, Y. Self-Assembly of Noble Metal Monolayers on Transition Metal Carbide Nanoparticle Catalysts. *Science.* **2016**, *352*, 974–978.

(13) Chen, W. F.; Muckerman, J. T.; Fujita, E. Recent Developments in Transition Metal Carbides and Nitrides as Hydrogen Evolution Electrocatalysts. *Chem. Commun.* **2013**, *49*, 8896–8909.

(14) Gong, Q.; Wang, Y.; Hu, Q.; Zhou, J.; Feng, R.; Duchesne, P. N.; Zhang, P.; Chen, F.; Han, N.; Li, Y.; Jin, C.; Li, Y.; Lee, S. T. Ultrasmall and Phase-Pure W_2C Nanoparticles for Efficient Electrocatalytic and Photoelectrochemical Hydrogen Evolution. *Nat. Commun.* **2016**, *7*.

(15) Li, C.; Zheng, M.; Wang, A.; Zhang, T. One-Pot Catalytic Hydrocracking of Raw Woody Biomass into Chemicals over Supported Carbide Catalysts: Simultaneous Conversion of Cellulose, Hemicellulose and Lignin. *Energy Environ. Sci.* **2012**, *5*, 6383–6390.

(16) Stellwagen, D. R.; Bitter, J. H. Structure-Performance Relations of Molybdenumand Tungsten Carbide Catalysts for Deoxygenation. *Green Chem.* **2015**, *17*, 582–593.

(17) Wu, H. Bin; Xia, B. Y.; Yu, L.; Yu, X. Y.; Lou, X. W. Porous Molybdenum Carbide Nano-Octahedrons Synthesized via Confined Carburization in Metal-Organic Frameworks for Efficient Hydrogen Production. *Nat. Commun.* **2015**, *6*, 1–8.

(18) Liu, R.; Pang, M.; Chen, X.; Li, C.; Xu, C.; Liang, C. W2C Nanorods with Various Amounts of Vacancy Defects: Determination of Catalytic Active Sites in the Hydrodeoxygenation of Benzofuran. *Catal. Sci. Technol.* **2017**, *7*, 1333–1341.

(19) Wang, H.; Liu, S.; Liu, B.; Montes, V.; Hill, J. M.; Smith, K. J. Carbon and Mo Transformations during the Synthesis of Mesoporous Mo2C/Carbon Catalysts by

Carbothermal Hydrogen Reduction. *J. Solid State Chem.* **2018**, *258*, 818–824.

(20) Nelson, J. A.; Wagner, M. J. High Surface Area Mo2C and WC Prepared by Alkalide Reduction. *Chem. Mater.* **2002**, *14*, 1639–1642.

(21) Souza MacEdo, L.; Stellwagen, D. R.; Teixeira Da Silva, V.; Bitter, J. H. Stability of Transition-Metal Carbides in Liquid Phase Reactions Relevant for Biomass-Based Conversion. *ChemCatChem* **2015**, *7*, 2816–2823.

(22) Yao, S.; Zhang, X.; Zhou, W.; Gao, R.; Xu, W.; Ye, Y.; Lin, L.; Wen, X.; Liu, P.; Chen, B.; et al. Atomic-Layered Au Clusters on α-MoC as Catalysts for the Low-Temperature Water-Gas Shift Reaction. *Science* **2017**, *357*, 389–393.

(23) Yao, Z.; Jiang, J.; Zhao, Y.; Luan, F.; Zhu, J.; Shi, Y.; Gao, H.; Wang, H. Insights into the Deactivation Mechanism of Metal Carbide Catalysts for Dry Reforming of Methane via Comparison of Nickel-Modified Molybdenum and Tungsten Carbides. *RSC Adv.* **2016**, *6*, 19944–19951.

(24) Lee, W.S.; Kumar, A.; Wang, Z.; Bhan, A. Chemical Titration and Transient Kinetic Studies of Site Requirements in Mo2C-Catalyzed Vapor Phase Anisole Hydrodeoxygenation. *ACS Catal.* **2015**, *5*, 4104–4114.

(25) Liu, P.; Rodriguez, J. A. Effects of Carbon on the Stability and Chemical Performance of Transition Metal Carbides: A Density Functional Study. *J. Chem. Phys.* **2004**, *120*, 5414–5423.

(26) Li, S.; Li, N.; Li, G.; Wang, A.; Cong, Y.; Wang, X.; Zhang, T. Synthesis of Diesel Range Alkanes with 2-Methylfuran and Mesityl Oxide from Lignocellulose. *Catal. Today* **2014**, *234*, 91–99.

(27) Jongerius, A. L.; Gosselink, R. W.; Dijkstra, J.; Bitter, J. H.; Bruijnincx, P. C. A.; Weckhuysen, B. M. Carbon Nanofiber Supported Transition-Metal Carbide Catalysts for the Hydrodeoxygenation of Guaiacol. *ChemCatChem* **2013**, *5*, 2964–2972.

(28) Bartholomew, C. H. Mechanisms of Catalyst Deactivation. *Appl. Catal. A Gen.* **2001**, *212*, 17–60.

(29) Fang, H.; Du, J.; Tian, C.; Zheng, J.; Duan, X.; Ye, L.; Yuan, Y. Regioselective Hydrogenolysis of Aryl Ether C–O Bonds by Tungsten Carbides with Controlled Phase Compositions. *Chem. Commun.* **2017**, *53*, 10295–10298.